Available online at www.sciencedirect.com
SCIENCE DIRECT®
Journal of Colloid and Interface Science 268 (2003) 143–153
JOURNAL OF Colloid and Interface Science
www.elsevier.com/locate/jcis

Porous glass electroosmotic pumps: design and experiments

Shuhuai Yao,[a] David E. Hertzog,[a] Shulin Zeng,[a] James C. Mikkelsen Jr.,[b] and Juan G. Santiago [a,*]

[a] *Department of Mechanical Engineering, Stanford University, Stanford, CA 94305, USA*
[b] *Department of Chemical Engineering, Stanford University, Stanford, CA 94305, USA*

Received 17 January 2003; accepted 17 July 2003

Abstract

An analytical model for electroosmotic flow rate, total pump current, and thermodynamic efficiency reported in a previous paper has been applied as a design guideline to fabricate porous-structure EO pumps. We have fabricated sintered-glass EO pumps that provide maximum flow rates and pressure capacities of 33 ml/min and 1.3 atm, respectively, at applied potential 100 V. These pumps are designed to be integrated with two-phase microchannel heat exchangers with load capacities of order 100 W and greater. Experiments were conducted with pumps of various geometries and using a relevant, practical range of working electrolyte ionic concentration. Characterization of the pumping performance are discussed in the terms of porosity, tortuosity, pore size, and the dependence of zeta potential on bulk ion density of the working solution. The effects of pressure and flow rate on pump current and thermodynamic efficiency are analyzed and compared to the model prediction. In particular, we explore the important tradeoff between increasing flow rate capacity and obtaining adequate thermodynamic efficiency. This research aims to demonstrate the performance of EOF pump systems and to investigate optimal and practical pump designs. We also present a gas recombination device that makes possible the implementation of this pumping technology into a closed-flow loop where electrolytic gases are converted into water and reclaimed by the system.

Keywords: Electroosmotic pump; Porous glass; Thermodynamic efficiency; Zeta potential; Catalytic recombination

1. Introduction

Electroosmosis refers to the bulk motion of an electrolyte caused by electric forces acting on regions of net charge in a microchannel. These net charge regions of diffuse ions make up part of the electric double layer (EDL) that forms at solid/liquid interfaces. Electroosmotic (EO) pumps use this effect to generate both flow rate and pressure differentials. In a previous paper [1], we have described the background and working principle of electroosmotic pumps and presented a detailed pump performance model. Our model yields analytical expressions for the electroosmotic flow rate, current, and thermodynamic efficiency of EO pumps with porous pumping structures operating under a pressure load. We treat electroosmotic flow (EOF) in porous media as flow through a large number of idealized tortuous microchannels in parallel. Key nondimensional parameters describing pump performance are summarized below. The nondimensional maximum flow rate, current, and pressure generated by a porous-structure EO pump are

$$Q^*_{\max} = \frac{\psi}{\tau} f E^*_{\text{eff}}, \tag{1}$$

$$I^*_{\max} = \frac{\psi}{\tau}\frac{f}{g} E^*_{\text{eff}}, \tag{2}$$

$$\Delta P^*_{\max} = f V^*_{\text{eff}}, \tag{3}$$

where

$$f = \int_0^a \left(1 - \frac{\varphi}{\zeta}\right)\frac{2r}{a^2}\,dr, \tag{4}$$

$$g = f \Bigg/ \left\{ \frac{\varepsilon^2}{\mu\sigma_\infty}\int_0^a \left(\frac{d\varphi}{dr}\right)^2 \frac{2r}{a^2}\,dr + \int_0^a \left[\frac{\Lambda_+}{\Lambda}\exp\left(-\frac{ze\varphi}{kT}\right) + \frac{\Lambda_-}{\Lambda}\exp\left(\frac{ze\varphi}{kT}\right)\right]\frac{2r}{a^2}\,dr \right\}. \tag{5}$$

$Q^*_{\max}$, $I^*_{\max}$, and $\Delta P^*_{\max}$ are nondimensionalized by $Q_{\max}\mu\lambda/(\varepsilon\zeta^2 A)$, $-I_{\max}\lambda/(\sigma_\infty\zeta A)$, and $\Delta P_{\max}a^2/(8\varepsilon\zeta^2)$, respectively. E^*_{eff} and V^*_{eff} are nondimensionalized respectively by

* Corresponding author.
E-mail address: juan.santiago@stanford.edu (J.G. Santiago).

0021-9797/$ – see front matter
doi:10.1016/S0021-9797(03)00730-6

$-V_{\text{eff}}\lambda/(\zeta L)$ and $-V_{\text{eff}}/\zeta$. The functions f and g are evaluated using solutions of the Poisson–Boltzmann (PB) equation.

Thermodynamic efficiency is defined as the useful pressure work delivered by the pump over the total power consumption. As both flow rate and current can be expressed as a function of pressure load, the thermodynamic efficiency can be then derived in terms of normalized pressure of the form $\Delta P' = \Delta P/\Delta P_{\max}$,

$$\eta = \frac{W_P}{V_{\text{app}} I} = \frac{\Delta P Q}{V_{\text{app}} I} = \frac{(1-\Delta P')\Delta P'}{(\theta/4) - \Delta P'}, \tag{6}$$

where

$$\theta = \frac{V_{\text{app}}}{V_{\text{eff}}} \frac{a^{*2}}{2\beta f g}. \tag{7}$$

For thin EDL systems, θ is much greater than unity, and a first-order-accurate approximation yields $\Delta P' = 0.5$ as the optimal pressure condition for the pump (i.e., the pressure load equals $\Delta P_{\max}/2$). The optimal thermodynamic efficiency is therefore approximately

$$\eta_{\text{opt}} \cong \frac{1}{\theta} = \frac{V_{\text{eff}}}{V_{\text{app}}} \frac{2\beta f g}{a^{*2}}. \tag{8}$$

Figure 1 shows a numerical solution of the nonlinear PB equation for electric potential which is valid for large zeta potential and accounts for the nonuniformity of ion conductivity across the flow areas of a porous pump [1].

The model described by Yao and Santiago [1] also leverages a curve fit of the GCSG site-binding model for the KCl/silica interface [2,3] to estimate the dependence of zeta potential on ion density and pH in our borosilicate-based system. This curve yields

$$\zeta = \big(-0.058\log_{10}(\text{pH}) + 0.026\big)\big(-\log_{10}(c_\infty)\big)^{1.02}. \tag{9}$$

This relation predicts the value given by the site-binding model to within 10% for ranges of ionic concentration from 10^{-4} to 10^{-2} M and pH values of 2.8 to 10.

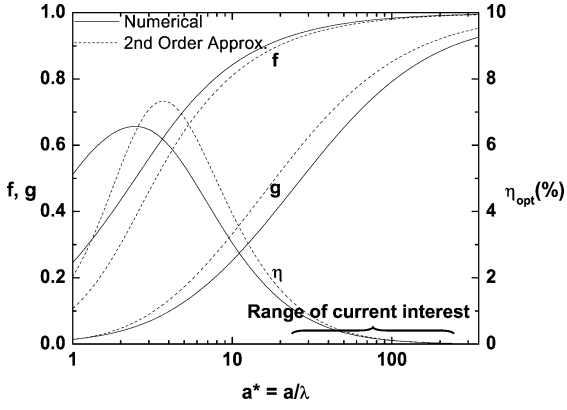

Fig. 1. Non-dimensional parameters f, g, and η_{opt}, as a function of nondimensional pore size. This plot is generated using sample parameter values of $\zeta^* = ze\zeta/(kT) = -3.9$ and $\beta = \varepsilon^2\zeta^2/(\mu\sigma_\infty\lambda^2) = 6.8$, assuming a typical zeta potential value of 100 mV. The range of nondimensional pore sizes of practical interest is 25 to 250.

We have used the model summarized above to guide the design of EO pumps for high-heat-load heat transfer applications. One important example is two-phase convection devices for electronic systems, which yield the highest cooling rates per unit volume of heat exchanger, but which require high-pressure pumping of the liquid phase. To date, the integrated circuit industry has lacked liquid pumps that are compact, reliable, and capable of delivering sufficient pressure [4]. EO pumps have demonstrated a capability to remove a total heat load exceeding 140 W from a silicon chip [5]. Further, cooling of peak heat fluxes exceeding 100 W/cm^2 from a silicon chip using less than 1.5 W of pump power has also been demonstrated [6].

In this paper, we present the design, fabrication, and testing of an electroosmotic pump system. We present detailed experimental validation of the performance of these pumps. We also compare the absolute performance values and trends predicted by the analytical model to these data. Our EO pump system uses a commercially available sintered-glass frit (ROBU Glasfilter-Geraete GmbH, Germany) as a porous medium for transporting the working fluid and generating high pressure. A buffered electrolyte (sodium borate buffer at pH 9.2) with ion concentrations varying from 0.2 to 4 mM is used to evaluate pump performance. In particular, we explore the important tradeoff between increasing flow rate capacity and obtaining adequate thermodynamic efficiency. This research aims to demonstrate the performance of EOF pump systems and to investigate optimal and practical pump designs. We also present a gas recombination device that enables the implementation of this pumping technology into a closed-flow loop where electrolytic gases are converted into water, which is then reclaimed by the system.

1.1. Effective pump voltage

To more accurately relate the DC electric potential supplied by the power supply, V_{app}, in our experiments to the pump potential, V_{eff}, in the equations above, we apply a simple potential model of the pump/electrode system. The voltage drop in the Joule current region between each electrode and the frit surface is equal to $R_d I$, where R_d is the resistance of this region and I is the system current. The expression for V_{eff} is therefore

$$V_{\text{eff}} = V_{\text{app}} - V_{\text{dec}} - 2R_d I. \tag{10}$$

Note that the effective potential's dependence of V_{app} is therefore a function of the fluidic load as I is a function of pressure difference across the pump. V_{dec}, in this relationship is the decomposition potential associated with the electrode reactions at the electrode/electrolyte surfaces of the system. This decomposition potential is the amount of voltage required to initiate the dissociation and association electrode reactions [7] and can be expressed as

$$V_{\text{dec}} = V_{\text{cat}} - V_{\text{an}} + V_o, \tag{11}$$

where V_{cat} and V_{an} are the theoretical potential differences required to initiate the Faraday current at the cathode and anode, respectively. V_o is the additional potential (called the overvoltage or overpotential) needed in practice to initiate the dissociation and association reactions at the electrodes (electrolysis) and is a function of electrode material, electrolyte composition, and electrodic current density. For our electrode/buffer combination, the magnitude of the $(V_{cat} - V_{an})$ was typically small in magnitude compared to V_{dec}. In comparing our measurements to pump model predictions of pressure and flow rate, we applied Eqs. (10) and (11) with measured values of system current, I, and decomposition potential, V_{dec}.

1.2. Catalytic recombination of hydrogen and oxygen

Any practical implementation of an electroosmotic pump needs to address the challenge of controlling electrolytic gas streams. The electrolytic reactions are required to sustain an electric field within the electrolyte-filled pump structure, and these reactions introduce mass fluxes of new species into the EO-pumped system. In our design we have chosen to work with simple, low ionic concentration aqueous buffers and inert platinum electrodes so that the electrode reactions are simply electrolysis of water with a net reaction of [8]

$$2H_2O \rightarrow 2H_2\ (g) + O_2\ (g).$$

Note that these gases are a small portion of the volume flow rate through the system. The volume flow rate of H_2 and O_2 in the system at a gas phase temperature, T, and pressure, P, can be estimated in terms of the Faradic current [7] as

$$Q_{H_2} = \frac{IkT}{2eP}, \tag{12}$$

$$Q_{O_2} = \frac{IkT}{4eP}, \tag{13}$$

where I is the total current supplied to the system. Using Eq. (24) from Yao and Santiago [1], the ratio of the total volume flow rate of (hydrogen plus oxygen) gas to the volume flow rate of water in a pump, γ, is then

$$\gamma = \frac{3\mu\sigma_\infty kT}{4\varepsilon\zeta ePg}. \tag{14}$$

For an electroosmotic pump with pore diameter 1.1 μm running with 1 mM (sodium ion concentration) borate buffer and a nominal zeta potential value of 100 mV, this volume flow rate ratio is 0.04 (assuming operation at 20 °C and pressure 1 atm). The ratio of hydrogen volume flow rate to liquid flow rate is 2.6%. Note that these conservative estimates of gas flow rates neglect gas dissolution into the electrolyte which may be significant.

In an open system where electrolysis gases are vented, this reaction will eventually consume the working liquid in the system. In a closed system, trapped gases increase system pressure and can block both current and mass flow. To deal with these gas generation issues, we have developed a catalytic recombination system that uses a platinum-based catalyst to recombine hydrogen and oxygen into liquid water. In the presence of platinum, the recombination reaction is simply

$$2H_2\ (g) + O_2\ (g) \xrightarrow{Pt} 2H_2O.$$

The evaluation of several candidate catalyst types and the performance of a packaged system are demonstrated in the results section below.

2. Device design and calibration experiments

The porous structure in our pumps was a chemically treated ultrafine glass frit (filter) (see Fig. 2a). The frit material is VitraPOR, borosilicate glass 3.3, which contains 80.60% silica (SiO_2), 12.60% boric oxide (B_2O_3), and 4.20% sodium oxide (Na_2O). Figure 2b is a scanning electron micrograph (SEM) of the porous glass pumping structure. The pores apparent in the image are on the order of a micrometer. Frit samples from two different fabrication batches from ROBU (S. Curland, ROBU Glasfilter-Geraete GmbH, Germany, personal communication) were used in our prototypes. These two batches (both UF 4-cm disks) will

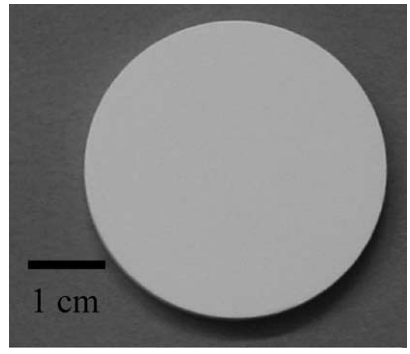

(a)

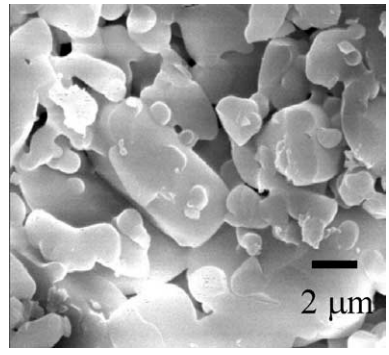

(b)

Fig. 2. Porous EO pumping structure. (a) Image of the pump structure, which is a 40-mm-diameter porous glass cylinder (a frit) 5 mm thick. (b) A scanning electron micrograph of the porous glass pumping structure. The observed pore sizes are on the order of 1 μm. This structure provides the high wetted-surface-to-volume ratio required to generate pressures exceeding 1.3×10^{-2} atm per volt.

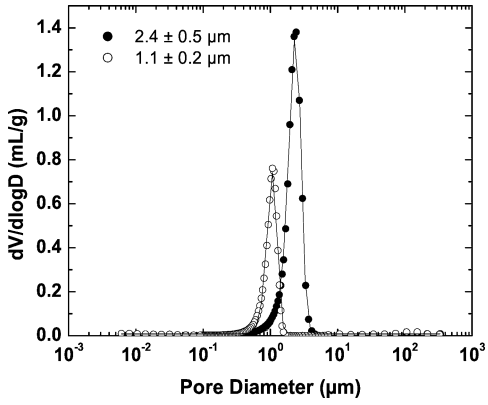

Fig. 3. Pore size distributions for two frit batches measured by an Autopore 9420 mercury porosimeter (Micromeritics, Norcross, GA). Pore diameter density is quantified here as the derivative of specific volume in ml/g with respect to the (base 10) logarithm of pore diameter [10]. Shown along with the data are Gaussian fitting functions. The mean pore diameters of the two samples are 2.4 ± 0.5 and 1.1 ± 0.2 μm.

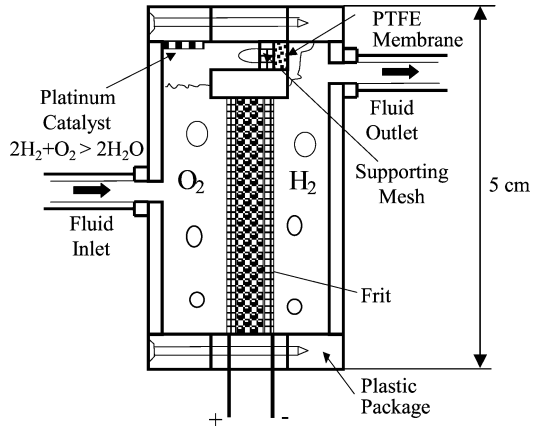

Fig. 4. Schematic of the EO pump system. A gas-permeable Teflon (PTFE) membrane allows most of the downstream hydrogen gas to bypass the fluidic circuit and flow into the catalytic chamber on the high-pressure side of the device. A platinum catalytic device housed within the pump structure recombines electrolytic hydrogen and oxygen gas into water, which is then reclaimed by the system.

Table 1
Characterization data of the frits

Frit	D (mm)	L_{ave} (mm)	a (μm)	ψ
L1	40.0	1.0	1.2	0.39
L2	40.0	2.5	1.2	0.39
L3	40.0	4.8	1.2	0.39
S1	40.0	1.0	0.55	0.24
S2	40.0	2.5	0.55	0.23
S3	40.0	4.8	0.55	0.22

be referred to here using the letters L and S (for "large" and "small" pore) and were selected because of their measurably different values of pore size and porosity in order to demonstrate the measurement and data reduction methods presented here. Figure 3 shows the distribution of pore sizes for a sample from each batch measured by a mercury intrusion porosimeter for both batches (J. Tripp, Department of Chemistry, University of California, Berkeley, personal communication). The mean pore diameters of the two samples are 2.4 ± 0.5 and 1.1 ± 0.2 μm. Porosity was determined by weighing dry and wet samples using a scale (ACCULAB, Newtown, PA); values ranged from 0.22 to 0.39. The diameter of all of the frits in this study was 40 mm. Frits of varying thickness were prepared by manually sanding frits from each of the two batches. Table 1 summarizes the characterization data of the frits including frit thickness, pore size (porosimeter measurement), and porosity (dry/wet weighing).

Figure 4 shows a schematic of our pump system showing the location of the porous (frit) pumping structure, electrodes, and fluidic connections. The pump housing was fabricated from plexiglass using a laser engraving and cutting system (Universal Laser Systems, Scottsdale, AZ). The frit is epoxied to a centerpiece which is then sealed with laser-machined rubber gaskets. Stainless steel tabulations from Scanivalve Corp. (Liberty Lake, WA) are used as quick-disconnect fittings to 1-mm-inner-diameter tubing. The platinum electrodes are located close to the frit surface but not attached, so that electrolysis bubbles would rise to the top of the chamber (rather than be advected into pores). The pump was used in an open loop configuration for detailed pressure, flow rate, and efficiency characterizations and in closed loop/sealed configuration for gas recombiner evaluation experiments.

The experimental setup for characterizing pump performance has been described in our previous work [9]. A Kepco power supply (Kepco Inc, Flushing, NY) provides an electric field across the electrodes of the pump. Pressure is measured downstream of the pump by a Digi-Key (Thief River Falls, MN) pressure transducer and the signal is collected by a digital multimeter (Agilent, Palo Alto, CA). Flow rate is measured by monitoring the motion of electrolytic bubble "slugs" in the output line of the pump. A control valve downstream of the pump is used to set desired pressure loads. The data acquisition system consists of a laptop computer with PCMCIA-GPIB and DAQCard-6062E (National Instruments, Austin, TX). Working electrolyte conductivity and pH are measured before each experiment using an ISFET pH meter (Cole-Parmer Instrument**,** Vernon Hills, IL) and a conductivity meter (Janco Instruments, San Diego, CA). In selected cases, electrolyte pH and conductivity were also monitored after experiments to verify the effectiveness of the borate buffer.

We have tested the EO pumps under a variety of buffer chemistries in order to optimize both flow capacity and Joule heating effect. The working fluid chemistries tested are listed in Table 2. The molarity values in the table indicate the molar concentration of sodium ions. As pointed out by Gan et al. [11], an effective buffer is essential to the stable operation of an EO pump, as ζ is a function of both pH and ionic density.

Two setups were used to evaluate the performance of the platinum catalyst structures designed to reclaim water from hydrogen and oxygen gas. A preliminary test cell for elec-

Table 2
Working fluids used in experiments (pH = 9.2)

Working fluid: $Na_2B_4O_7$ (mM based on Na^+)	Conductivity (S/m)
0.2	1.42×10^{-3}
0.4	2.98×10^{-3}
0.6	4.58×10^{-3}
0.8	6.23×10^{-3}
1.0	7.73×10^{-3}
1.2	9.49×10^{-3}
1.4	1.10×10^{-2}
1.6	1.25×10^{-2}
1.8	1.39×10^{-2}
2.0	1.55×10^{-2}
3.0	2.23×10^{-2}
4.0	2.98×10^{-2}

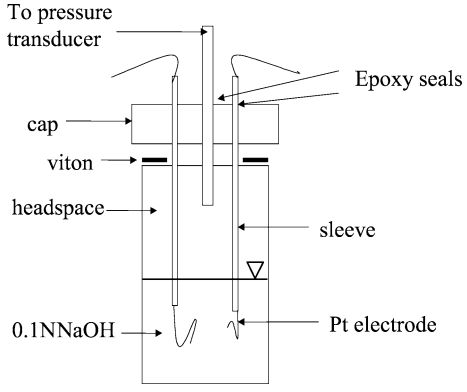

Fig. 5. Schematic of electrolysis pressure cell. A sealed glass container 1 cm in diameter has three ports at the top for two electrodes and a pressure tap. A Viton gasket and epoxy seal the top and electrode connections. Partially sleeved platinum electrodes are used to generate hydrogen and oxygen in a 0.1 N NaOH solution. Candidate catalyst materials are suspended in the head space with a plastic mesh.

trolysis gas pressure measurements is shown in Fig. 5. A vial cap was modified to contain Pt wire feed-throughs for electrodes. The Pt wires were covered with polyethylene sleeves in the headspace to minimize any catalytic reactions on bare Pt wire surfaces. A "cage" was fabricated from polyethylene mesh, hung from the sleeved electrodes, and used to hold catalyst samples. A Viton gasket, which was coated with silicone vacuum grease, was used to ensure a tight seal between the vial and the cap. Samples of each catalyst were loaded into the cage, the cap tightened, the voltage applied, and the gas pressure monitored with the transducer. The second setup used to evaluate catalyst performance is shown in Fig. 4 (see also the insert schematic of Fig. 13, which is discussed below). Here, a custom-designed platinum catalytic system housed within the pump structure recombines electrolytic hydrogen and oxygen gas into water, which is then reclaimed by the system. A gas-permeable Gore-Tex expanded polytetrafluoroethylene (PTFE) membrane on spunbonded polypropylene with 0.45-μm pores (W.L. Gore & Associates, Inc., Elkton, MD) allows most of the hydrogen gas generated at the cathode (on the downstream side of the pump) to bypass the fluidic circuit and flow into the catalytic recombination chamber. We used AECL catalyst manufactured by Atomic Energy Canada Limited (Mississauga, Canada) in a closed loop to observe electrolysis operation for periods in excess of 5 h.

3. Experimental results and discussion

Preliminary calibration experiments were conducted to evaluate the value of the resistance per length of the electrolyte in our electrode/housing structure. Current increases linearly with the applied voltage for a 4-cm-diameter, 6-mm-thick void cell with 1 mM (sodium ion concentration) borate buffer. The decomposition potential of the platinum/electrolyte interface is estimated from this experiment as 4.5 V. The measured resistivity is 205 Ω/mm. As discussed above, the pump's electrical current is also a function of load and concentration. As such, the value of V_{eff} for each experiment is determined by applied voltage, decomposition potential, spacing resistance and current (using Eq. (10)). This process is simplified by the fact that the values of overpotential and the spacing between the electrode and the frit surface, d, were in all cases within about 10% of the nominal 4.5 V and 1 mm, respectively, and these values were therefore assumed constant.

Maximum pump flow rate, $Q_{\max}$, maximum pump current, $I_{\max}$, and maximum pump pressure, $\Delta P_{\max}$, were characterized at external applied voltages of 5 to 100 V, using a borate buffer with a 1 mM Na^+ concentration. These experiments were performed in open-loop configurations where gases were vented. Figure 6 shows the effects of applied field and potential on the measurements of these nondimensional parameters. The nominal pump field (V_{eff}/L) and voltage drop values (V_{eff}) shown here were calculated using Eq. (10) as described above. The scales for the nondimensionalization of flow rate and current were 5.4×10^4 ml/min and 100 A, respectively. The characteristic scale for pressure was 39 N/m^2 for the 2.4-μm pore diameter frits and 184 N/m^2 for the 1.1-μm pore diameter frits. Data are shown for six different frits comprising three frit thickness and two pore sizes. As predicted by Eqs. (1)–(3), flow rate and current have a linear dependence on the electric field, while pressure depends linearly on the effective voltage. This linear dependence on field and voltage in a nearly isothermal pump operation regime was also documented by Zeng et al. [12] for packed capillary electroosmotic pumps. In all experiments, the slope of the plot depends on the structure of the frits as characterized by pore size a, porosity, ψ, and tortuosity, τ. The scaling proposed here collapses these data clearly into two groups corresponding to the nondimensional pore sizes $a_1^* = 125$ and $a_2^* = 57$. The factors of $f(a^*)$ for these two batches are 0.99 and 0.97, respectively, while the corresponding values for $g(a^*)$ are 0.83 and 0.68 (see Fig. 1). In Fig. 6a, the slopes of the linear fit of the pump flow rate to the electric field are 0.22 and 0.11 for large- and small-pore frits,

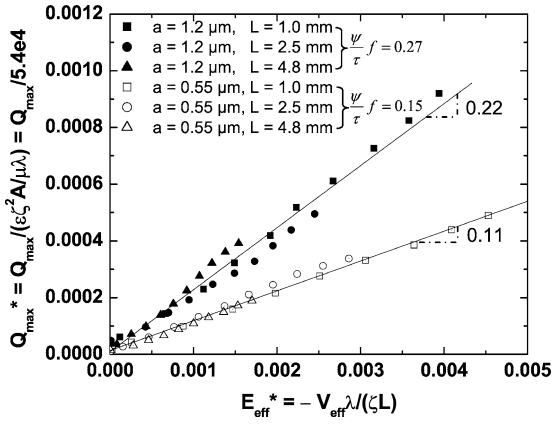

(a)

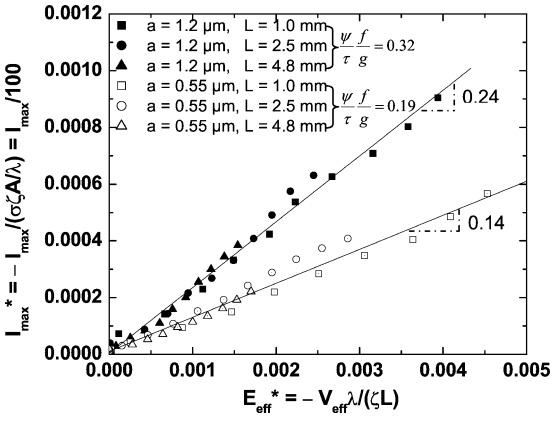

(b)

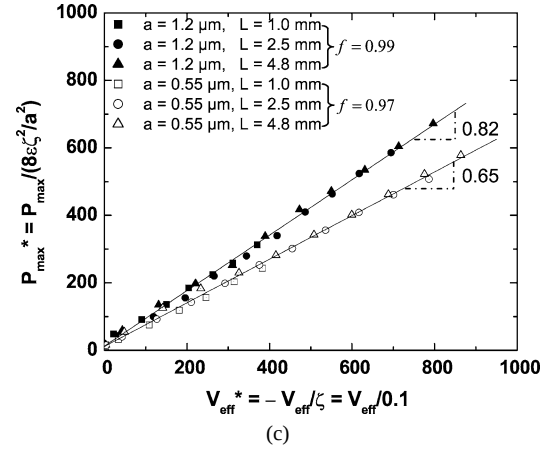

(c)

Fig. 6. Normalized flow rate, current, and pressure performance of pump across variations in pump length, pore size, and applied potential. In all cases, working fluid is 1 mM (sodium ion concentration) borate buffer (pH 9.2, $\sigma_\infty = 77$ μs/cm) and applied voltages ranged from 5 to 100 V (yielding respective effective voltages ranging from 0.5 to 86 V). (a) Nondimensionalized flow rate versus nondimensionalized electric field. (b) Nondimensionalized current versus nondimensionalized electric field. (c) Nondimensionalized pressure versus nondimensionalized effective voltage, showing how data group into two batches of frits. These data are all linear with respect to the value of the abscissa, as predicted by Eqs. (1)–(3). Shown in the legend are values for ψ/τ as determined by preliminary calibration experiments, f and g from numerical solution of PB equation (see Fig. 1). The small and large pore sizes correspond to values of $a_1^* = 125$ and $a_2^* = 57$.

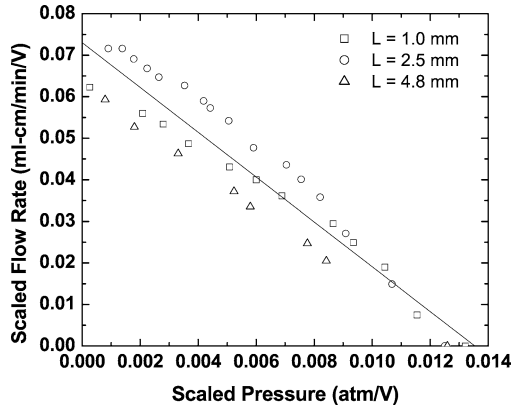

Fig. 7. Pressure load characterization shown as scaled flow rate versus pressure per volt for three pumps of the batch with pore radius 0.55 μm and three thicknesses. Working fluid is 1 mM (sodium ion concentration) borate buffer (pH 9.2, $\sigma_\infty = 77$ μs/cm). These pumps were able to deliver a maximum flow rate excess of 7×10^{-2} (ml cm)/min/V and a maximum pressure of 1.3×10^{-2} atm/V.

respectively, compared to the corresponding values of 0.27 and 0.15 obtained from the model predictions (see the legend). Similarly, Figs. 6b and 6c show the two sets of data of current–field and pressure–voltage relationship. The numerical model overpredicts the absolute flow rate, total current, and pump pressure by, respectively, 23%, 33%, and 21% in the case of the 2.4-μm pore diameter frits, and by 36%, 36%, and 49% in the case of the 1.1-μm pore diameter frits. Part of this discrepancy may be due to the fact that the model assumes a cylindrical pore with a single pore diameter, while the actual porous frit is composed of randomly shaped glass particles, resulting in pores of complex shape and a polydisperse characteristic diameter distribution (see Fig. 3).

The measured values of $Q_{\max}$ and $\Delta P_{\max}$ allow the estimation of tortuosity as described by Yao and Santiago [1]: $\tau_1 = 1.45 \pm 0.11$ and $\tau_2 = 1.45 \pm 0.05$, where the uncertainties reflect 95% confidence intervals for a distribution of 12 realizations. The collapsed data highlights the utility of the porous medium flow model and, in particular, the importance of the ratio ψ/τ in the characterization of porous pump performance.

The pressure-to-flow-rate ratio is perhaps the most important descriptor of pump performance. Figure 7 shows the scaled flow rate vs the scaled pressure of the small-pore frit (batch S with $a_2 = 0.55$ μm) for thicknesses of 1.0, 2.5, and 4.8 mm. For a given applied potential, flow rate is inversely proportional to frit thickness and pressure remains constant, as predicted by Eqs. (1) and (3). An important consideration for designers of large-flow-rate EO pumps is the flow rate and pressure achieved by a design for a given applied voltage. The best voltage specific performance of our pumps is, as expected, achieved by the 1-mm-thick frit pump, which demonstrated a flow rate of 20 ml/min and a maximum pressure of 0.4 atm for an applied voltage of 50 V. The flow rate per unit applied voltage and unit area performance is 3×10^{-2} (ml/min)/V/cm^2. This figure of merit can be

compared to the values of 1×10^{-3} (ml/min)/V/cm^2 and 6×10^{-4} (ml/min)/V/cm^2 reported by Zeng et al. [13] and Gan et al. [11], respectively. In the case of the pump described by Zeng et al. [13], this performance value was hindered by the two 5-mm-thick polymeric porous frits used to contain their silica particle bed, which reduced the effective electrical field across their pump. The pump used by Gan et al. [11] was 13 mm thick along the flow direction, and so also suffered from low effective field within the pumping region. Next, the pressure per unit applied voltage performance of the pumps described here is approximately 1×10^{-2} atm/V. This value can be compared to the high-flow-rate porous borosilicate glass pumps developed by Gan et al. [11], which demonstrated a pressure limit of 3×10^{-3} atm/V. This pressure performance was limited mostly by their relatively large pore diameter range of 2–5 μm. The pump fabricated by Zeng et al. [13] demonstrated a pressure per applied voltage value of 2×10^{-3} atm/V which, as they discuss, was limited mostly by the pressure drop in the polymeric frits of their device.

Clearly, the model discussed by Yao and Santiago [1], the results presented above, and comparisons with other high-flow-rate EO pumps demonstrate that thin pumps provide optimal voltage specific performance characteristics. To date, we do not know the limiting factors on thinning frit pumps. Certainly one physical limitation on this design approach is the breakdown strength of water, which is given by Zahn et al. as 15 kV/mm [14]. Note that a thin pump used for two-phase cooling applications would most likely be subject to electrical potentials higher than about 10 V in order to preserve pressure capacity. A second fundamental limit on minimum porous structure thicknesses is the finite length scale of the sintered/packed particles used to create the structure (particle scales of 1–5 μm were used in the frits described here). As pump thickness approaches the characteristic dimension of the particles, the structure is expected to become highly heterogeneous over the cross-sectional area of the frit. In our design, the most important limitation on pump thickness is the structural strength of the free-standing frit structure (see Fig. 4). The two-phase heat transfer applications of interest here require significant (>0.2 atm) operating pressures. The development of thinning methods and structural support structures applicable for use with ultrathin (say 0.1 mm or less) frits would be an important contribution to this field.

As shown by Eqs. (4), (5), (8), and (9) and Fig. 1, electrolyte ionic concentration has an important impact on pump flow rate, pressure, and thermodynamic efficiency through the characteristics of the (finite) electrical double layers and the zeta potential's dependence on concentration. In our regime of interest, the 1 mM (Na^+) buffer used in the experiments above provided frit pumps with nearly maximum flow rate per field while maintaining efficiencies to within an acceptable level for our applications. For example, throughout the regime of interest highlighted in Fig. 1, increases in concentration decrease thermodynamic efficiency while

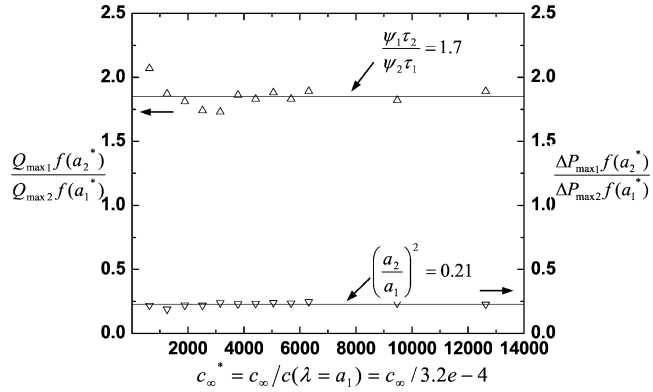

Fig. 8. Ratios of maximum flow rate and maximum pressure for the pumps with $a_1 = 1.2$ μm and $a_2 = 0.55$ μm (both with a thickness of 4.8 mm). Borate buffer concentrations vary from 0.2 to 4 mM (Na^+) as described in Table 2. The constant ratio relationship predicted by Eqs. (15) and (16) is shown along with the experimental data. The measured values of $\psi_1\tau_2/\psi_2\tau_1$ and $(a_2/a_1)^2$ are within 9.5% and 9.0%, respectively, of the values based on the model and preliminary (independent) calibration experiments.

increasing both pressure and flow rate. In order to validate our choice of buffer concentration, investigate these trends, and further compare the frits of the two batches, we performed a series of experiments in which we characterized pump performance as a function of borate buffer concentration. Twelve concentrations of borate buffer (see Table 2) were tested for two 4.8-mm-thick frits with pore radius $a_1 = 1.2$ μm and $a_2 = 0.55$ μm.

From Eqs. (1) and (3), we can derive the following relationships for the ratios of maximum flow rate and maximum pressure capacity for these two frits:

$$\frac{Q_{\max 1}}{Q_{\max 2}} = \frac{\psi_1\tau_2}{\psi_2\tau_1}\frac{f(a_1^*)}{f(a_2^*)}, \tag{15}$$

$$\frac{\Delta P_{\max 1}}{\Delta P_{\max 2}} = \frac{a_2^2}{a_1^2}\frac{f(a_1^*)}{f(a_2^*)}. \tag{16}$$

These relationships are especially interesting as neither of them depends on zeta potential, so that the dependence on porosity, tortuosity, and pore size is emphasized. These ratios of maximum flow rate and maximum pressure are shown in Fig. 8. The buffer ionic concentration is nondimensionalized as $c_\infty^* = c_\infty/c(\lambda = a_1)$, where $c(\lambda = a_1) = 3.2 \times 10^{-4}$ mM. a^* varies from 25 to 250 and the integral factor f varies from 0.93 to 0.99 over this respective range. Buffer ionic concentrations substantially lower than 0.2 mM ($a^* < 25$) were not presented here, as the electrolyte pH of such runs was unstable and dropped appreciably in the upstream region of the pump during testing. The data in Fig. 8 are shown along with line plot predictions for $\psi_1\tau_2/\psi_2\tau_1$ and a_2^2/a_1^2, which are derived strictly from the preliminary calibration experiments described earlier (including wet and dry weight, current, pressure, and porosimeter measurements).

Figure 9 shows zeta potentials calculated using maximum flow rate and maximum current measurements, and the ana-

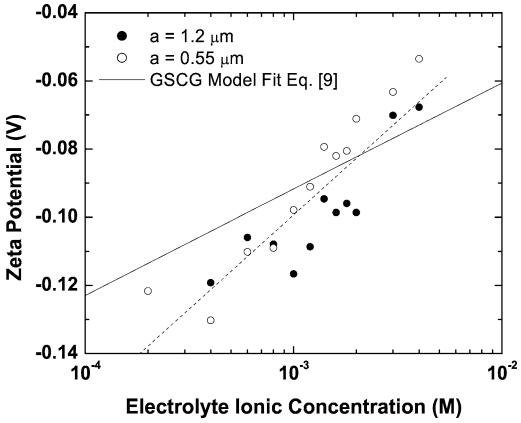

Fig. 9. Trend of measured zeta potential versus concentration for the porous EO pumps. Data are shown for both frit batches. Shown together with the experimental data is a prediction using the simple curve fit to the GCSG model for the KCl/silica model (solid line) calculated using Eq. (9). Also shown with the data is a linear regression fit to the data (dashed line), which shows that the zeta potential measurements scale approximately as $c_\infty^{-0.3}$ (where c_∞ is concentration). The KCl/silica model underpredicts the influence of concentration of zeta potential, but both experimental and model data clearly show a dependence that is weaker than the simple $c_\infty^{-0.5}$ dependence predicted by the simple Gouy–Chapman model.

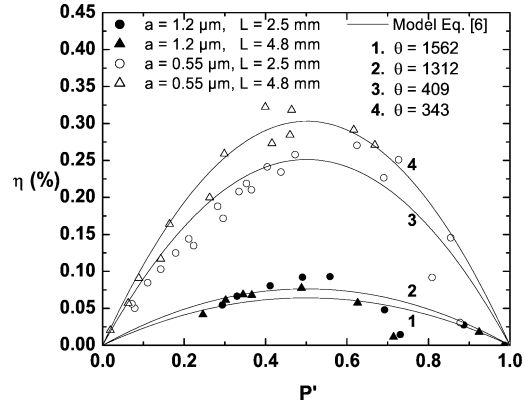

Fig. 10. Pump thermodynamic efficiency as a function of pressure. Experiments were conducted at 100 V with 1 mM (sodium ion concentration) borate buffer (pH 9.2, $\sigma_\infty = 77$ μs/cm). The experimental data were calculated using measured values of I, Q, and ΔP. Shown together with the experimental data are model prediction based on Eq. (6). θ is estimated by Eq. (7) and the results of the preliminary calibration experiments.

lytical expression for $Q_{\max}/I_{\max}$ equal to $-\varepsilon\zeta g/(\mu\sigma_\infty)$ [1]. These measurements are obtained for our borosilicate frit surfaces, which are in contact with borate buffer at various ionic concentrations. We compared the experimental results to the GCSG model [2] described above. As an approximate basis of comparison, the modeling parameters suggested by Scales et al. [3] for KCl-on-silica surfaces at pH 9 were used. As described by Yates et al. [2], our data show a dependence on concentration that is clearly weaker than that predicted by a simple Gouy–Chapman diffuse EDL model with constant surface density at the shear plane [15]. The measured zeta potential values are scattered about a mean value of approximately 100 mV; they are comparable to the data of Scales's experiment for KCl on silica. Our experimental data show a slightly stronger dependence of zeta potential on concentration than the prediction of the GSCG model, but the dependence is clearly weaker than the Gouy–Chapman prediction.

3.1. Thermodynamic efficiency

Thermodynamic efficiency as a function of pressure was investigated for pumps of varying pore radius and thickness. Experiments were conducted at 100 V with 1 mM (Na^+) borate buffer (pH 9.2, $\sigma_\infty = 77$ μs/cm). We compared the experimental data with our model prediction, as shown in Fig. 10. The experimental data were calculated from the definition in Eq. (6) and direct measurements of flow rate, current, and pressure. The experimental data are shown together with the predictions given by Eq. (6). The values of θ are 1562, 1312, 409, and 343 for the experiments shown. The experimental data are in good agreement with the model prediction, with the exception of data in the high-backpressure region. Because of the recirculating nature of the flow in this regime, the pump operates at a temperature a few degrees higher than for the high-flow-rate operation. As predicted for θ values significantly greater than unity [1], the optimal pressure condition for thermodynamic efficiency is approximately $\Delta P' = 0.5$. The thermodynamic efficiency is highly dependent on the pore radius, a (scaling as $1/a^2$), and has only a weak dependence on the thickness, L.

The thermodynamic efficiency for varying buffer concentrations has also been investigated. The borate buffer concentrations listed in Table 2 were used at 100-V applied potentials for two pumps with pore diameters $a_1 = 1.2$ μm and $a_2 = 0.55$ μm (both with thickness 4.8 mm). Again, efficiency is determined directly using measurements of pressure, flow rate, voltage, and current. Shown together with these efficiency measurements are predictions based on Eqs. (8)–(10). In this buffer range, θ varies between 92 and 1.3×10^4, so that, to first-order accuracy, the optimal pressure condition for thermodynamic efficiency is near $\Delta P' = 0.5$. Again, note that buffer concentrations significantly below 0.1 mM were impractical because pump operation generated prohibitively large fluctuations in pH. In this calculation, we use a Debye length based on the concentration of sodium ions in solution (consistent with our symmetric electrolyte approximation) and the measured bulk conductivity. Both experimental data and predictions made using this approach are shown in Fig. 11. As predicted by the model, thermodynamic efficiency increases steadily with decreasing ionic strength in the range of interest (see Fig. 1). The model successfully captures the effect of pore size on scaling efficiency.

The thermodynamic efficiency data highlight another important design issue: the tradeoffs between pH stability, thermodynamic efficiency, and absolute pressure and flow rate performance of a frit pump. We have found that a practical lower limit on ion density for our borate buffer is approximately 0.2 mM ionic concentration (required to preserve

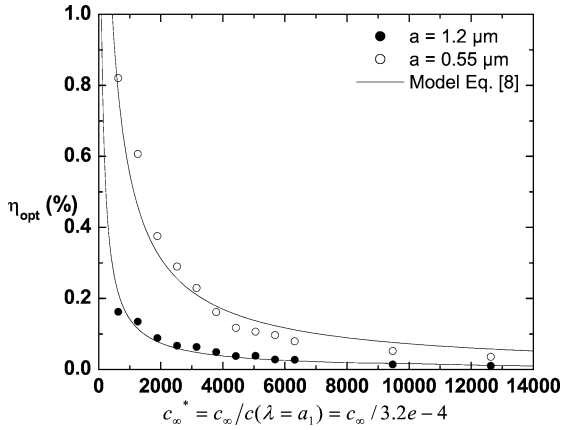

Fig. 11. Optimal pump thermodynamic efficiency (obtained here at the $\Delta P = \Delta P_{\max}/2$ point) as a function of nondimensionalized electrolyte ionic concentration. Borate buffer concentrations vary from 0.2 to 4 mM (Na^+) as described in Table 2. Experimental data are shown for two pumps with pore sizes $a_1 = 1.2$ μm and $a_2 = 0.55$ μm, both with thickness 4.8 mm. Solid lines are model predictions from Eq. (8) for the two cases.

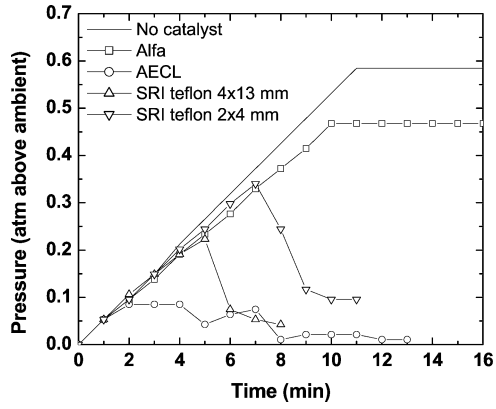

Fig. 12. Initial tests of three types of catalysts with a source current of 50 mA in the closed test cell shown in Fig. 5. The test cell was half-filled with 0.1 N NaOH solution, leaving a headspace of about 13 ml in which the gas would collect and increase pressure above ambient. Approximately 5 V was applied across a pair of Pt electrodes. The Faradic current produced approximately 0.65 ml/min gas at standard temperature and pressure. The best-performing catalyst was the material manufactured by Atomic Energy of Canada Limited, which kept the pressure of the cell below 0.1 atm.

pH stability in the region just upstream of the pump). For the 1 mM buffer we chose for many of the experiments in our paper, we have observed steady-state pump performance consistent with our models for long term (>24-h) experiments. The thermodynamic efficiency data of Fig. 1 suggest that the peak point of optimal thermodynamic efficiency would occur at $a^* = 2.5$. At the minimum practical ionic density, this translates to a pore diameter of 0.1 μm, so that smaller pores are favorable to increase pressure performance. However, such a pump not only is difficult to fabricate but would have significantly reduced absolute flow rate performance because of the effects of finite electrical double layers. For example, for equal geometry and surface chemistries, such a pump is expected to deliver 4×10^{-2} (ml cm)/min/V (flow rate per field) and 1.1 atm/V (pressure per voltage), which can be compared to the corresponding 7×10^{-2} (ml cm)/min/V and 1.3×10^{-2} atm/V values for our prototype pump (4-cm frit labeled S in Table 1). For a designer of practical pumped-loop systems, there is therefore an important tradeoff of absolute pump pressure and flow rate performance versus required power for any given pump size. This tradeoff will be particularly important in potential portable applications of this technology such as two-phase cooling of laptop computers or fluid pumping applications in handheld devices.

3.2. Gas recombination device characterization

Lastly, we present an evaluation of our gas recombination approach. Two experiments were performed. First, a set of experiments were performed in a closed reaction cell to compare the performance of several catalyst materials, and second, a demonstration of the implementation of the gas control and recombination components shown in Fig. 13 was performed for a pump in a closed-loop system operating with a finite pressure load. The results of the first experiment are shown in Fig. 12. Four candidate platinum-based catalyst materials selected were (1) 1/8″ Pt-coated aluminum ceramic beads commercially from Alfa Aesar (Ward Hill, MA); (2) beads provided by Atomic Energy of Canada Limited; (3) a platinum/carbon elastomeric sheet test sample; and (4) Pt-coated carbon mesh, commercially available from Electrosynthesis (Lancaster, NY). The figure shows the pressure of the test cell as a function of time for a current of 50 mA. In this simple experiment, the Electrosynthesis material showed no catalytic activity up to 1.5 atm (data not shown). We found the Alfa catalyst(s) to be ineffective in recombining, as evidenced by the increasing pressure of 0.5 atm. In repeated tests of the SRI–Teflon sample, a pressure decrease was observed and consistently related to the dimension of the sample sheet, which is indicative of catalytic activity. The best-performing catalyst was the material manufactured by Atomic Energy of Canada Limited. For this material, after an initial increase in pressure to 0.1 atm, the cell pressure decreases as gas recombination was activated. These results suggest that, in general, catalyst requires an activation pressure before working effectively (at least with catalysts initially at room temperature). One important result from these experiments is a validation of the importance of the hydrophobicity of the catalyst material surface. As H_2 and O_2 recombine, the reaction product (water) tends to form a film on the catalyst. For relatively hydrophilic materials (e.g., bare platinum), this water film prevents further exposure of reactants to platinum. An important aspect of the AECL catalyst is that the (tailored) hydrophobic nature of the material's surface promotes beading of the water, which then drops off the catalyst and exposes new surface.

The results of the second catalyst experiment are shown in Fig. 13. The AECL catalyst was integrated into the pump device and placed within a closed fluidic loop system as shown schematically in Fig. 13. The plot shows gauge cham-

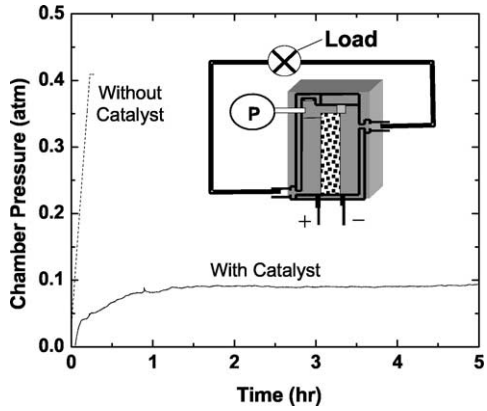

Fig. 13. System pressure in a hermetically sealed closed-loop pump test with and without a sample of the AECL catalysis demonstrating the effectiveness of the catalytic recombination and gas control system. Without catalyst the experiment was terminated when the system gauge pressure rose to 0.4 atm; with catalyst, the system gauge pressure was maintained below 0.1 atm.

ber pressure under steady-state electrolysis for 5 h at 10 mA. Without a catalyst in the system, the absolute system pressure of this closed loop rises quickly to more than 0.4 atm (gauge) where the experiment is terminated. With a catalyst, the sealed closed-loop system maintains a pressure under 0.1 atm for more than 5 h. In these experiments the pressure level upon deactivation of the pump electrodes was monitored in order to verify that the leak are rate of gases to the environment was negligible.

The pressure differential across the load valve in the closed-loop catalyst experiments was about 0.1 atm (approximately 10% of the pump's maximum pressure capacity). For a newly fabricated system, the membrane successfully bypassed the hydrogen gas into the upstream section of the pump. However, after the system ran for a few days, the membrane showed signs of fouling and/or degradation and was less effective. This resulted in a condition where some of the hydrogen generated at the cathode did not pass through the membrane but exited through the outlet tube and flowed through the fluidic loop to the upstream side of the pump (where it then recombined with oxygen). In all cases, hydrogen and oxygen re-combined in the upstream region of the pump and the system pressure remained constant as shown in Fig. 13. We are currently reevaluating the design and performance of the gas control system.

4. Conclusions

Sintered porous glass EO pumps have been designed and fabricated. The pump performance has been characterized experimentally and compared to a theoretical model presented by Yao and Santiago [1]. The nondimensional scaling suggested by the model was shown to adequately collapse pump performance data including pressure, flow rate, and efficiency across variations in geometry (including pore size and pump length), voltage, electric field, and ionic concentration. The numerical model overpredicts the absolute flow rate, total current, and pump pressure by, respectively, 23%, 33%, and 21% in the case of the 2.4-μm pore diameter frits, and by 36%, 36%, and 49% in the case of the 1.1-μm pore diameter frits. At least part of this discrepancy may be due to the random geometry of pores in the glass frit structure, which is clearly different from the idealized cylindrical pore geometry of the model and has a polydisperse pore size distribution. Future work will be aimed at resolving this discrepancy between our porous structure model and pump performance. The model is an excellent predictor of performance trends and is therefore useful to designers of EO pump systems. The model can be used to design operation potential and working electrolyte ionic concentration given preliminary calibration experiments to determine pore size, porosity, tortuosity, and electrode/pump coupling characteristics (including overpotential and electrode-to-frit spacing). This design process is particularly useful in weighing the tradeoffs between pH stability, absolute pressure and flow rate performance, thermodynamic efficiency, and structural strength of the frit material. Given these insights and our own empirical observations of pump performance, we have been able to design a compact and fairly robust device able to provide a pressure and flow rate capacity applicable to high-heat-load cooling. For example, one of our prototype pumps (with an active pumping structure volume of less than 2 cm^3) can generate maximum flow rates and pressure capacities of 33 ml/min and 1.3 atm, respectively, at 100 V.

We have also demonstrated several packaging and gas control strategies for the implementation of EO pumping technologies. The design uses gas-permeable Teflon membranes to allow cathodic hydrogen gas to bypass the pump output flow stream and combine directly with oxygen gas produced on the upstream, low-pressure side of the pump. On this low-pressure side, the system uses a platinum-based catalytic recombination device to recombine of the electrolytic gases to liquid water. A 5-h test with the catalyst showed that the sealed closed-loop system kept the pressure under 0.1 atm.

Acknowledgments

This work was supported by DARPA under Contract F33615-99-C-1442 and by Intel Corporation. We also appreciate the help of Dr. Jennifer Tripp in providing the porosimeter measurements of our frits.

Appendix A. Nomenclature

A	Cross-sectional area (m^2)
E	Electric field ($V\,m^{-1}$)
I	Current (A)
L	Length (m)
L_e	Average length along the pore path (m)
P	Pressure (Pa)

ΔP	Pressure capacity (Pa)
Q	Flow rate (ml min^{-1})
R_d	Resistance of electrode-to-frit space (Ω)
V	Potential (V)
W_P	Pressure work (W)
$\forall$	Total volume of the porous medium (m^3)
$\forall_e$	Void volume of the porous medium (m^3)
a	Pore radius (m)
c_∞	Electrolyte concentration (M)
e	Elementary charge (C)
k	Boltzmann constant (J K^{-1})
n_∞	Electrolyte number concentration (m^{-3})
r	Radial coordinate (m)
z	Charge number (–)
Λ	Molar conductivity (S m^2 mol^{-1})
β	Nondimensional advective current parameter (–)
ε	Permittivity of liquid (C V^{-1} m^{-1})
γ	Gas-to-liquid volume flow rate ratio (–)
η	Thermodynamic efficiency (–)
θ	Nondimensional efficiency parameter (–)
λ	Debye length, $\lambda = (\varepsilon kT/2e^2z^2n_\infty)^{0.5}$ (m)
μ	Viscosity (Pa s)
σ_∞	Electrolyte conductivity (S m^{-1})
φ	Electrical potential (V)
ζ	Zeta potential (V)
τ	Tortuosity, $\tau = (L_e/L)^2$ (–)
ψ	Porosity, $\psi = \forall_e/\forall$ (–)

Subscripts

an	Anode
app	Applied value
cat	Cathode
dec	Decomposition
eff	Effective value
max	Maximum value
o	Overpotential (overvoltage)
opt	Optimal value
$+$	Cation
$-$	Anion

References

[1] S. Yao, J.G. Santiago, submitted for publication.
[2] D.E. Yates, S. Levine, T.W. Healy, J. Chem. Soc. Faraday Trans. 74 (1974) 1807.
[3] P.J. Scales, F. Grieser, T.W. Healy, Langmuir 8 (1992) 965.
[4] L. Jiang, J.C. Mikkelsen, J.-M. Koo, D. Huber, S. Yao, L. Zhang, P. Zhou, J.G. Maveety, R. Prasher, J.G. Santiago, T.W. Kenny, K.E. Goodson, IEEE Trans. Comp. Packag. Manufact. Technol. 25 (3) (2002) 347.
[5] L. Jiang, J.-M. Koo, L. Zhang, E. Wang, S. Im, S. Yao, S. Zeng, A. Bari, J.G. Santiago, T. Kenny, K.E. Goodson, in: Proc. 4th PaRTSEE Workshop, Kyoto, 2002.
[6] K.E. Goodson, J.G. Santiago, T. Kenny, L. Jiang, S. Zeng, J.-M. Koo, L. Zhang, S. Yao, E. Wang, Electron. Cooling 8 (2002) 46.
[7] J.O'M. Bockris, A.K.N. Reddy, Modern Electrochemistry: An Introduction to an Interdisciplinary Area, 1st ed., Plenum, New York, 1970.
[8] R.H. Perucci, W.S. Harwood, General Chemistry: Principles and Modern Applications, Macmillan, New York, 1993.
[9] S. Yao, S. Zeng, J.G. Santiago, in: Proc. ASME IMECE Microfluidics Symposium, New Orleans, 2002.
[10] G. Herdan, Small Particle Statistics, Elsevier, Amsterdam/Houston, 1953.
[11] W. Gan, L. Yang, Y. He, R. Zeng, M.L. Cervera, M. de la Guardia, Talanta 51 (2000) 667.
[12] S. Zeng, C.H. Chen, J.C. Mikkelsen, J.G. Santiago, Sens. Actuat. B 79 (2–3) (2001) 107.
[13] S. Zeng, C.H. Chen, J.G. Santiago, J. Chen, R.N. Zare, J.A. Tripp, F. Svec, J. Fréchet, Sens. Actuat. B 82 (2–3) (2001) 209.
[14] M. Zahn, Y. Ohki, D.B. Fenneman, R.J. Gripshover, V.H. Gehman, Proc. IEEE 74 (1986) 1182.
[15] R.J. Hunter, Zeta Potential in Colloidal Science: Principles and Applications, Academic Press, London, 1981.